

Magnetic and Velocity Field Topology in Active Regions of Descending Phase of the Solar Cycle 23

R. A. Maurya¹ · A. Ambastha²

© Springer ●●●●

Abstract

We analyse the topology of photospheric magnetic fields and sub-photospheric flows of several active regions (ARs) that are observed during the peak to descending phase of the solar cycle 23. Our analysis shows clear evidence of hemispheric preferences in all the topological parameters such as the magnetic, current and kinetic helicities, and the ‘curl-divergence’. We found that 68%(67%) ARs in the northern (southern) hemisphere with negative (positive) magnetic helicities. Same hemispheric preference sign is found for the current helicities in 68%(68%) ARs. The hemispheric preferences are found to exist statistically for all the time except in few ARs observed during the peak and the end phases of the solar cycle. This means that magnetic fields are dominantly left(right)-helical in scales smaller than individual ARs of northern(southern) hemisphere. We found that magnetic and current helicities parameters show equator-ward propagation similar to the sunspot cycle. The kinetic helicity showed similar hemispheric trend to that of magnetic and current helicity parameters. There are 65%(56%) ARs with negative (positive) kinetic helicity as well as divergence-curl, at the depth of 2.4 Mm, in the northern (southern) hemisphere. The hemispheric distribution of the kinetic helicity becomes more evident at larger depths, *e.g.*, 69%(67%) at the depth of 12.6 Mm. Similar hemispheric trend of kinetic helicity to that of the current helicity supports the mean field dynamo model. We also found that the hemispheric distribution of all the parameters increases with the field strength of ARs. The topology of photospheric magnetic fields and near surface sub-photospheric flow fields did not show good association but the correlation between them enhances with depths which could be indicating more aligned flows at deeper layers of ARs.

Keywords: Helioseismology: observations, Helicity: Current, Magnetic; Active Regions: Magnetic Fields, Velocity Field; Solar Cycle: Observations

1. Introduction

Solar active regions are three-dimensional magnetic structures extending from the interior below the photosphere to the coronal heights. They consist of magnetic flux tubes that emerge from the convection zone and extend into the solar atmosphere (Hood, Archontis, and MacTaggart, 2011, and references therein). Solar interior near the photosphere is an excellent conductor where frozen-in-field condition may satisfy (Priest, 2014). Over a period of time, near the photosphere, plasma flows may evolve with magnetic field lines, and may swirl around them. A flux tube emerging from the convection region is prevented from being

✉ R. A. Maurya
ramajor@nitc.ac.in

✉ A. Ambastha
ambastha@prl.res.in

¹ Department of Physics, National Institute of Technology Calicut, Calicut-673601, India.

² Udaipur Solar Observatory, Physical Research Laboratory, Udaipur-313001, India.

destroyed by the hydrodynamics vortex behind it when twisting effects are present (Fan *et al.*, 1998). Therefore, we can expect topological association between the sub-photospheric flows and photospheric magnetic fields.

Mathematically, the topology of a vector field \mathbf{X} is represented by the parameter ‘‘helicity’’. It is defined by the volume integral of the scalar product of the vector field and its curl, $\mathbf{Y} = \nabla \times \mathbf{X}$,

$$H = \int_V \mathbf{X} \cdot \mathbf{Y} \, dV. \quad (1)$$

The helicity is a fundamental topological quantity in laboratory as well as in astrophysical plasma. In general, helicity (Equation 1) describes what kind of handedness is preferable for the field \mathbf{X} , left or right hand screw. If $\nabla \times \mathbf{X}$ is clockwise when viewed from ahead of the body, then helicity is positive; and if counter-clockwise, it is negative. The helicity defined in Equation 1 is a global parameter over the entire volume V .

The magnetic helicity of a divergence-free field \mathbf{B} within a volume V , bounded by a surface S , is defined by (Elsasser, 1956),

$$H_m = \int_V \mathbf{A} \cdot \mathbf{B} \, dV \quad (2)$$

where, the vector potential \mathbf{A} satisfies, $\mathbf{B} = \nabla \times \mathbf{A}$. However, Equation 2 is gauge invariant (independent of ϕ where $\mathbf{A}' = \mathbf{A} + \nabla\phi$) when the magnetic field is fully contained inside the volume V . The helicity H_m is a measure of linking, knotting and twisting of field lines (Moffatt, 1969; Berger and Field, 1984). Note that there is a subtle mathematical difference between the general definition of the helicity H (Equation 1) and the magnetic helicity H_m (Equation 2). In the definition of the helicity H of the field \mathbf{X} , we integrate the scalar product of the field \mathbf{X} with its curl, while for the helicity H_m of magnetic field \mathbf{B} , we integrate the scalar product of vector potential \mathbf{A} of magnetic field \mathbf{B} (and NOT \mathbf{B} itself) with its curl. This makes difficult to compute the magnetic helicity, as the vector potential \mathbf{A} is gauge invariant and the full 3D magnetic fields are not observable. Therefore, force-free parameter α_f given in the equation,

$$\nabla \times \mathbf{B} = \alpha_f \mathbf{B}, \quad (3)$$

is taken as a proxy for the magnetic helicity by several researchers (Pevtsov *et al.*, 2008, and references therein). The topology of flow fields can be given by the kinetic helicity (Moffatt and Tsinober, 1992; Moffatt, 1969). It is defined as the volume integral of the scalar product of velocity (\mathbf{u}) and vorticity $\boldsymbol{\omega}$,

$$H_k = \int_V \mathbf{u} \cdot \boldsymbol{\omega} \, dV \quad (4)$$

where, vorticity, $\boldsymbol{\omega} = \nabla \times \mathbf{u}$, is another important topological parameter to describe the flow which represents circulation per unit area or twist of fluid fields. It is a pseudo-vector (or axial vector) that transforms like a vector under a proper rotation, but in three dimensions again an additional sign flip occurs under an improper rotation such as a reflection. Note that H_k retains the same mathematical form for the flow field \mathbf{u} as of H for the vector field \mathbf{X} . It represents extent to which corkscrew-like motion occurs. If a parcel of fluid is moving and rotating about an axis parallel to the direction of motion, it will be positive. In the absence of complete velocity field observations, we compute the kinetic helicity density,

$$h_k = \mathbf{u} \cdot \boldsymbol{\omega} = \mathbf{u} \cdot \nabla \times \mathbf{u}, \quad (5)$$

as a proxy for the swirls in the sub-photospheric flows. The kinetic helicity density, h_k , is a scalar quantity and it represents the component of vorticity along the direction of flow. In magneto-hydrodynamics, the kinetic helicity of flow field has similar mathematical form as that of the ‘‘current helicity’’,

$$H_c = \int \mathbf{J} \cdot \mathbf{B} dV \quad (6)$$

where, \mathbf{J} is current density which is related with magnetic field by formula, $\mathbf{J} = \frac{1}{\mu_0} \nabla \times \mathbf{B}$, and $\mu_0 = 4\pi \times 10^{-7} \text{ Hm}^{-1}$ is the permeability of free space. The current helicity quantifies the location of twist and sheared non-potential structures in a magnetic field of ARs. It defines the degree of twist and linkage of electric currents. Since full 3D magnetic fields are not observed, we consider the current helicity density as follow,

$$h_c = (\nabla \times \mathbf{B}) \cdot \mathbf{B}. \quad (7)$$

It is evident from Equation 2 and 6 that only current helicity density can be estimated from the vector magnetograms under the assumption of non-linear force-free field, and the calculation of magnetic helicity density can only be made under the more restrictive assumption of constant α_f of force-free field. However, the force-free parameter α_f has the same sign as that of magnetic field under the assumption of linear force field (Hagyard and Pevtsov, 1999). They are related by the formula, $h_c = \alpha_f B_z^2$ (Seehafer, 1990), which implies that for a given AR, the current helicity has same sign as that of the magnetic helicity. However, in a recent study, Russell *et al.* (2019) conjectured that current and magnetic helicities having the same sign is not true in general.

In the solar chromosphere, magnetic structures such as H_α vortices, filament chirality, *etc.*, manifest the existence of helicity in ARs. The topology in all the above features demonstrate a consistent pattern relating a large scale ordering of solar magnetic fields. From a study of chromospheric H_α images of 51 sunspots from 1901 to 1944, Hale (1927) first reported the preference of hemispheric trend in the H_α vortices. Later, Richardson (1941) included some more sunspots and reported 71% (66%) with left-handed (right-handed) vortices in the northern (southern) hemisphere. The hemispheric sign rule (HSR) has also been found in the chirality of chromospheric filaments (*e.g.*, Martin, Bilimoria, and Tracadas, 1994; Pevtsov, Balasubramaniam, and Rogers, 2003; Lim and Chae, 2009).

Vector magnetic field observations of solar ARs have revealed that on average solar ARs have a small but statistically significant mean twist and they show hemispheric biases. The magnetic helicity (Pevtsov, Canfield, and Metcalf, 1995; Longcope, Fisher, and Pevtsov, 1998; Bao, Ai, and Zhang, 2000; LaBonte, Georgoulis, and Rust, 2007; Yang, Zhang, and Büchner, 2009; Zhang and Yang, 2013; Liu, Hoeksema, and Sun, 2014) and the current helicity (Seehafer, 1990; Bao and Zhang, 1998; Abramenko, Wang, and Yurchishin, 1996; Pevtsov, Canfield, and Latushko, 2001; Hagino and Sakurai, 2005; Gosain *et al.*, 2013, among others) of ARs have been found to follow HSR. However, opposite HSR in the global force free parameter α_f has been reported earlier during the beginning (Bao, Ai, and Zhang, 2000) and decay phases (Tiwari, Venkatakrishnan, and Sankarasubramanian, 2009; Pipin *et al.*, 2019) of solar cycles. From an analysis of several ARs, Zhang (2006) pointed out that the ARs with strong magnetic fields show opposite hemispheric trend. Pevtsov *et al.* (2008) compared data from four different instruments and concluded that HSR sign change in some phases of the solar cycle is not supported at high level of significance. Choudhuri, Chatterjee, and Nandy (2004) have numerically shown the hemispheric preference of magnetic helicity parameter α_f . They also noticed opposite HSR at the beginning of solar cycle. However, there is also some debate about this rule.

Twist in a magnetic flux tube can be formed due to: (1) Coriolis force acting on rising flux tube (Holder *et al.*, 2004) and Σ -effect (Longcope, Fisher, and Pevtsov, 1998). The Coriolis force tilts one leg of the tube towards equator and the other away. This deformation generates helical distortion in the tube's central axis. (2) Flux tube buffeted by the turbulence of convection outside the tube during its rise through the convection zone. The kinetic helicity of the turbulent flows in convection zone twists the rising flux tube. (3) Background poloidal field (Choudhuri, 2003; Choudhuri, Chatterjee, and Nandy, 2004). The magnetic helicity is expected to change its sign too because flows drags field lines with it (Gilman, 1983). Longcope, Fisher, and Pevtsov (1998) showed fluid motion with right handed coil deform the flux tube with a left handed.

Using helioseismic measurement of sub-photospheric flows, Komm *et al.* (2007) have reported cyclonic vorticity (counter clockwise) in the northern hemisphere. The hemisphere preference has also been found in other studies (Gao, Zhang, and Zhao, 2009; Maurya, Ambastha, and Reddy, 2011; Seligman, Petrie, and Komm, 2014; Komm, Gosain, and Pevtsov, 2014). There are a few studies on the combined topology of sub-photospheric flows and photospheric magnetic helicities (Gao, Zhang, and Zhao, 2009; Maurya, Ambastha, and Reddy, 2011; Seligman, Petrie, and Komm, 2014; Komm and Gosain, 2015). In some of these studies, kinetic helicity has been found to show statistically opposite HSR than that of current helicities (Gao, Zhang, and Zhao, 2009).

There are not enough studies reported on the topology of the combined photospheric magnetic fields and sub-photospheric velocity fields from the peak to descending phase of the solar cycle 23. Therefore, it would be interesting to investigate the topological parameters of sub-photospheric flows, photospheric magnetic fields and their hemispheric preferences, associations. With this aim, we explore for any possible relationship between the magnetic and kinetic helicities using photospheric vector magnetograms and Dopplergrams observations of a large sample of ARs. Rest of the manuscript is organized as follow: In Section 2, we describe the selection of ARs and the observational data used. We discuss the methodology for computing different helicity parameters. Section 3 is devoted to the results and discussion, and finally, we present the summary and conclusions in Section 4.

2. The Active Regions, Data and Analysis

The main observational data used in this study consists of dopplergrams and vector magnetograms of several ARs of the main to decay phase of the solar cycle 23. Doppler observations of the full disc Sun for several years are available from the Global Oscillation Network Group (GONG) while the corresponding vector magnetic field observations are not available as such during the aforementioned period. Therefore, for our studies, we have obtained vector magnetograms from the Marshall Space Flight Center (MSFC). Furthermore, GONG high resolution Doppler observations are available from 22 July 2001 onward while MSFC vector magnetograms are available only for the periods 19 September 2000 to 25 October 2004. Due to this constraint, we have chosen only the common sets of data for the period of 22 July 2001 to 25 October 2004. The other limitations are the availability of daily vector magnetic field data. There are data gaps of several days. ARs far away from the disc center suffer from the foreshortening effects (Maurya, Ambastha, and Chae., 2014, and references therein) and produce spurious results in helioseismic computations. Hence, we selected only the ARs within the radius of $\pm 40^\circ$ in heliographic longitude and latitude. In total, we short-listed 189 ARs for the common period of MSFC and GONG observations, where some of these ARs were observed during multiple rotations. In our sample of 189 ARs, 118 ARs were found to be located in the southern hemisphere and 71 ARs in the northern hemisphere. Thus the number of ARs for the southern hemisphere is larger than that in the northern hemisphere. However, we do not expect our results on HSR to be statistically affected by the different numbers of ARs in the two hemispheres.

2.1. The Vector Magnetograms and Analysis

The MSFC vector magnetograph facility was assembled in 1973 to support the Skylab mission, and thereafter went through several improvements (MSFC, Hagyard *et al.*, 1982; Hagyard and Kineke, 1995; West *et al.*, 2002). The vector magnetic fields data were taken in the magnetically sensitivity spectral line Fe I 5250.2 Å using the Zeiss birefringent filter with band pass of 125 mÅ. Its spatial resolution over the $7' \times 5.2'$ field-of-view is $0.64'' \text{pixel}^{-1}$. These observations are taken in the far wing of the spectral line at -90 mÅ (or -120 mÅ) from the line center, where the Faraday rotation effect decreases (Ronan *et al.*, 1992). The pixel resolution of the MSFC magnetograms is $1''.28$ along both x- and y-directions.

The MSFC observations consist of line-of sight magnetic field (B_t), transverse component (B_t) and the azimuth angle (ϕ) of B_t . The horizontal components (B_x, B_y) of the vector magnetic field can be computed from B_t and ϕ . We resolved the usual 180° ambiguity in the transverse components from all the vector magnetograms using the acute angle method

although there are several other methods available as reviewed by Metcalf *et al.* (2006). Further, to avoid any projection effects, we transformed the images to the disc center using the method described by Venkatakrisnan and Gary (1989).

The MSFC vector magnetograms are not aligned in the east-west and north-south directions which should be corrected for comparing the photospheric magnetic fields with sub-photospheric flows obtained from the GONG. Active region's NOAA number and their central locations are provided in the header of every vector magnetogram. However the central coordinates are found to be incorrect in some cases. In order to correct the coordinates and orientation of the MSFC vector magnetograms, we have used the full disc SOHO/MDI magnetograms for reference. First of all, based on the location and time provided in the header of the vectors magnetograms, we estimated corresponding location in the MDI magnetograms and then after cross-correlating the ARs between MSFC and MDI magnetograms, we corrected for the locations and orientations of MSFC observations.

2.1.1. Determination of Magnetic and Current Helicities

As discussed in the Section 1, the force-free parameter α_f (Equation 3) can be used as a proxy for the magnetic helicity (Equation 2). But, \mathbf{B} is observed only at a single height, so we can have its derivatives only along x - and y - directions. Thus, we can compute only the vertical part of α_f . Basically, there are two approaches for calculating it: *i*) $(\alpha_f)_{\text{best}}^z$ which is the best fit single value for the whole AR in the least squares sense (Pevtsov, Canfield, and Metcalf, 1995), and *ii*) $(\alpha_f)_{\text{av}}^z$ which is the average of the vertical component of α_f over the entire AR (Bao and Zhang, 1998; Abramenko, Wang, and Yurchishin, 1996; Hagino and Sakurai, 2004). Both methods have been found to be in fairly good agreement to each other (Leka and Skumanich, 1999). For a linear force-free field, the values of α_f for a given position (x, y) , can be given by,

$$\alpha_f^z(x, y) = \frac{\sum J_z \cdot B_z}{\sum B_z^2} = \left[\sum_{x,y} \left(\frac{\partial B_y}{\partial x} - \frac{\partial B_x}{\partial y} \right) \cdot B_z \right] / \sum_{x,y} B_z^2 \quad (8)$$

where, numerical derivatives of magnetic field components can be determined using the Lagrange's three point interpolation. While computing the pixel values of $\alpha_f^z(x, y)$ in an AR, we selected only those pixels where the total magnetic field strength were above the quiet regions. To get the net twist in an AR, we took average over the entire AR,

$$(\alpha_f^z)_{\text{av}} = \frac{1}{N} \sum_{x,y} \alpha(x, y) \quad (9)$$

where, N represents the total number of points where $\alpha_f^z(x, y)$ are estimated. Along with the magnetic helicity parameter $(\alpha_f^z)_{\text{av}}$, we computed the vertical current helicity,

$$(h_c^z)_{\text{av}} = \frac{1}{N} \sum_{x,y} J_z \cdot B_z = \frac{1}{N} \sum_{x,y} \left(\frac{\partial B_y}{\partial x} - \frac{\partial B_x}{\partial y} \right) B_z \quad (10)$$

We have also computed the net absolute magnetic flux (B) for every AR by adding the fluxes for those positions where helicity is estimated. From the above expressions for the magnetic helicity parameter α_{av}^z (Equation 9) and current helicity parameter h_c^z (Equation 10), it is evident that both these parameters could have same sign for a given AR.

2.2. Sub-photospheric Flows

The horizontal components (u_x, u_y) of the sub-photospheric flow parameters for all ARs are computed from the Doppler observations using the ring-diagram analysis (Hill, 1988). The basis of this method is that the frequency of sound waves inside the solar interior are perturbed by the sub-photospheric plasma motion, $\delta\omega_{n,\ell} = \mathbf{k}_{n,\ell} \cdot \mathbf{U}_{n,\ell}$, where, $\mathbf{k}_{n,\ell}$ is the propagation vector and $\mathbf{U}_{n,\ell}$ is the flow vector for a given mode (n, ℓ) . Mode parameter $\mathbf{U}_{n,\ell}$ can be computed by fitting the three dimensional Doppler power spectra (Haber *et al.*,

2000). It is related with the sub-photospheric flows, $\mathbf{U}_{n,\ell} = \int K_{n,\ell}(r)\mathbf{u}(r)dr + \epsilon_{n,\ell}$, where the kernel $K_{n,\ell}$ can be computed based on standard solar model (Christensen-Dalsgaard *et al.*, 1996), $\mathbf{u}(r)$ is the horizontal velocity at radius r , and $\epsilon_{n,\ell}$ is the error in the mode parameter $U_{n,\ell}$. This is an inverse problem, Fredholm equation of first kind, which can be solved using inversion methods such as regularized least squares (Gough, 1985). For more detail about the ring-diagram analysis one can refer to the review paper by Antia and Basu (2007).

The sub-photospheric flows are largely affected by the solar differential rotation and meridional circulations. We computed the residual flows by removing these large scale trend following the methods as described in Komm *et al.* (2004).

Ring-diagram yields only the horizontal components, u_x and u_y , of the flow, but not the vertical component, u_z , at any point in the interior. We estimated the u_z from the divergence of horizontal components, assuming mass conservation (Komm *et al.*, 2004), or steady-state continuity equation,

$$\frac{\partial \rho(z)u_z}{\partial z} + \rho(z)(\nabla \cdot \mathbf{u})_h = 0, \quad (11)$$

with horizontal divergence,

$$div_h \equiv (\nabla \cdot \mathbf{u})_h \equiv \frac{\partial u_x}{\partial x} + \frac{\partial u_y}{\partial y}. \quad (12)$$

Note that z is the vertical height increasing with radial distance with the origin on the surface. The interior is specified by a negative value of z . By supposing u_z on the surface, $z = 0$, and integrating the continuity Equation 11 over z from d (negative) to 0, we obtain,

$$u_z(d) = -\frac{1}{\rho(d)} \int_0^d \rho(z)(\nabla \cdot \mathbf{u})_h dz \quad (13)$$

which has the same form as Equation (5) of Komm *et al.* (2004). Now, suppose $(\nabla \cdot \mathbf{u})_h > 0$ in the height range from d to 0, then it follows that $u_z(d) > 0$. This means that a horizontally diverging flow rises upward, and hence u_z and $(\nabla \cdot \mathbf{u})_h$ are expected to have the same sign.

2.2.1. Sub-photospheric Topological Parameters

Following, Equation 10 for the current helicity, we computed the vertical kinetic helicity density as follow,

$$h_k^z = \langle u_z \cdot \omega_z \rangle \quad (14)$$

where, the vertical vorticity is given by,

$$\omega_z \equiv curl_z = \frac{\partial u_y}{\partial x} - \frac{\partial u_x}{\partial y}, \quad (15)$$

represents the twist of the flow around the vertical (radial direction). The parameter h_k^z is analogous to h_c (Equation 7), and we have taken it as a proxy for the kinetic helicity density.

Note that the vertical kinetic helicity density h_k^z (Equation 14) is obtained from the weighted average of ω_z by u_z . But one should note that in strong magnetic field regions vertical flows are suppressed due to the Lorentz force. The horizontal divergence (Equation 12) of flows from the sunspot regions to outwards are common. Therefore, weighted average of ω_z with div_h would be a better estimate for the vertical helicity. Such a parameter can be given by,

$$C_k^z = \langle div_h \cdot curl_z \rangle \quad (16)$$

The parameter, C_k^z , is expected to have same sign as that of h_k^z because div_h and u_z are expected to have same sign as explained earlier. This expression for the vertical twist has been

used earlier for studying the kinetic helicity of supergranular flows (Egorov, Rüdiger, and Ziegler, 2004) and sub-photospheric flows (Komm *et al.*, 2007). The validity of above helicity proxy has been confirmed for the depth range obtained from ring-diagram as numerically established by Miesch *et al.* (2008).

In order to compute the sub-photospheric flow topological parameters for an AR, we first computed them over patches of $60^\circ \times 60^\circ$ around the disc center. Then the parameters associated with the ARs were interpolated based on their coordinates on the solar disc.

Earlier studies (Komm *et al.*, 2005; Maurya, Ambastha, and Tripathy, 2009; Maurya and Ambastha, 2010) have shown bipolar structure of sub-photospheric flows in several ARs. Therefore, two different types of twists are possible in the underlying flows of ARs. To deal with it, we analysed h_k^z and C_k^z at the two depths of 2.4 Mm and 12.6 Mm. For distribution, the associated parameters are labeled by the subscripts ‘1’ and ‘2’, *e.g.*, h_{k1}^z and h_{k2}^z , respectively.

The sub-photospheric flows of ARs are obtained from the 1664 minute time-series duration with a cadence of one-minute Doppler observations and thus correspond to average subsurface flows over a day. Therefore, for comparing magnetic field topology with sub-photospheric flows of an AR, the magnetic field topological parameters are also averaged accordingly.

Note that, next section onward, we have used the vertically averaged quantities only, and therefore, we have dropped the scripts “z” and “av” from all the topological parameters, *e.g.*, we have used h_c instead of $(h_c)_{av}^z$.

3. Results and Discussion

Results of our analysis of the 189 ARs are shown in Figures 1 – 11. The hemispheric distribution of topological parameters are summarized in the Tables 1 and 2.

3.1. Photospheric Magnetic Fields

The photospheric magnetic field topology is studied in terms of magnetic helicity parameter α_f (Section 3.1.1) and current helicity h_c (Section 3.1.2). In the following, we discuss the results obtained.

3.1.1. Magnetic Helicity

The results of our analysis for the magnetic helicity parameter α_f are shown in Figures 1 – 3. Figure 1(a) shows the latitudinal distribution of magnetic helicity parameter α_f for the 189 ARs. We found 68%(67%) ARs in the northern (southern) hemisphere with negative (positive) α_f . This result further confirms the earlier reports on HSR for the magnetic helicity. We notice that α_f shows large scatter in both the hemispheres. Therefore, the following questions arise: Is the hemispheric sign statistically significant? How do α_f values vary with latitude?

To address the above questions, we fitted a linear regression model through the parameters α_f . In Figure 1(a), the solid line shows the linear regression line while dashed curves correspond to the 95% confidence ($\sim 2\sigma$) interval. The confidence interval 95% contains the best-fit regression line. The fitted line has a slope, $-3.4 \times 10^{-10} m^{-1} degree^{-1}$, such that the magnitude of α_f increases with latitude. However, linear regression is not fully satisfactory because we do not have any known reason for the straight line to be the appropriate fit. But at the same time, we can not justify higher order polynomials. The average values of α_f in northern (southern) hemisphere is found to be $-4.7(+7.6) \times 10^{-9} m^{-1}$.

To examine the statistical significance of hemispheric trend, we calculated probability distribution function (PDF) for α_f which is shown in Figure 1(b). The peak of density function for northern (southern) hemisphere lies at $-5.4(+3.4) \times 10^{-8} m^{-1}$. These results confirm the hemispheric trend of the estimated α_f values for our set of ARs. The FWHM of PDF of α_f for northern (southern) hemispheric points is $2.3(2.6) \times 10^{-8} m^{-1}$. That is, α_f of the southern hemisphere is spread slightly more than that of the northern hemisphere.

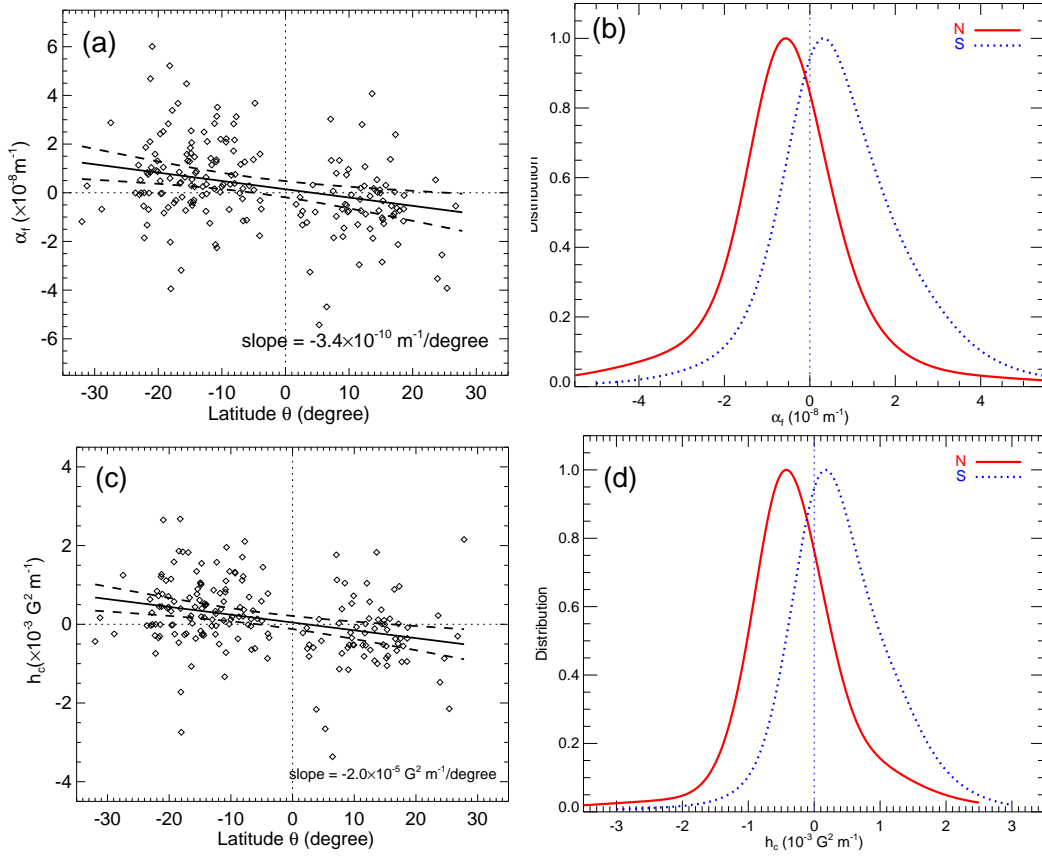


Figure 1. (a) Latitudinal distribution of the force-free parameter α_f , where solid lines represent the linear least square fitting between the parameter α_f and latitude, while the dashed curves correspond to 95% confidence intervals. (b) Probability distribution function of the parameter α_f for the northern hemisphere (solid & red) and southern hemisphere (dotted & blue). Bottom row is similar to the top row but for the current helicity h_c .

Next we address whether ARs of different magnetic field strengths have similar twist in their field lines. For this, we plotted the magnetic field parameter α_f as a function of absolute magnetic flux (B) in Figure 2(a). In this plot, we have only shown the data points with $|\alpha_f| \geq 0.5 \times 10^{-8} \text{ m}^{-1}$ for clarity. A linear regression is performed through positive and negative values of α_f of ARs. The values of slope of the regression is found to be $+5.6(-5.8) \times 10^{-11} \text{ m}^{-1} \text{ G}^{-1}$ for positive (negative) α_f . This result shows that the ARs with stronger magnetic fields have larger twist irrespective of ARs's hemispheric locations.

Figure 2(b) shows magnetic field related HSR in the helicity parameter α_f . For this, we ran a boxcar magnetic flux of size 50 G, and counted ARs following the HSR as a function of B . Linear regressions through the data are shown with dashed lines with a slope 0.06(0.10). This implies that the HSR becomes stronger with magnetic fields strength of ARs.

Next, we explore the time dependent hemispheric trend of the magnetic helicity parameter α_f (Figure 3). Figure 3(a) shows the monthly averaged sunspot number as a function of time; in the period where ARs are taken for this paper. A complete solar cycle 23 is also shown in the inset of the top panel where vertically dotted lines mark the time window over which ARs are taken for this analysis. This period corresponds to the peak to the descending phase of the solar cycle 23.

Magnetic helicity parameter α_f for the northern and southern hemisphere is plotted in Figure 3(b). The symbols with opened (filled) circles represent negative (positive) values of the magnetic helicity parameter α_f . This panel not only shows the predominantly hemispheric distribution of the parameter α_f but also part of the butterfly-diagrams for sunspots which indicates that the sunspots appear at larger latitude in the beginning of solar cycle and as time passes they appear at lower latitude as shown by the linear regression lines (dashed) through ARs latitudes.

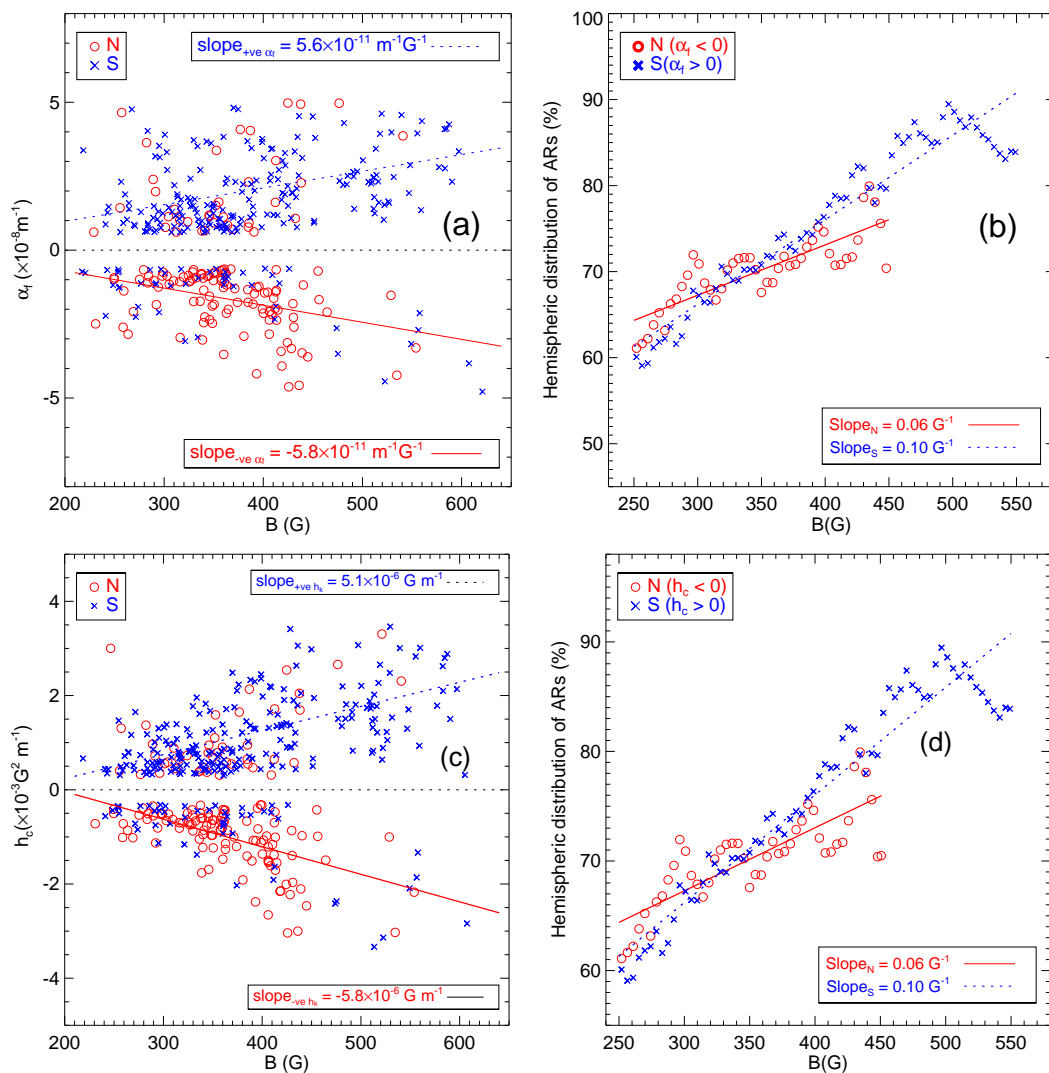


Figure 2. (a) The helicity parameter α_f as a function of absolute magnetic flux of ARs. Solid (dashed) line below (above) $\alpha_f = 0$ represents the linear least square fitting through northern (southern) data points. The slopes of the fitted lines are mentioned within the rectangular boxes. (b) Hemispheric distribution of ARs based on α_f values as a function of magnetic field. The dashed (solid) lines represent the linear regression for the northern (southern) ARs. Corresponding equations are given in the rectangular boxes. Bottom row is similar to the top row but for the current helicity h_c .

These distributions show a clear indication of the hemispheric distribution of the magnetic helicity in both the northern and southern hemispheres. Around the end of year 2002, there are ARs with slightly large magnetic helicity. During the end phase of the solar cycle, the magnetic helicity reduces, as is obvious from the smaller circles. Overall, there seems to be equator-ward propagation of the magnetic helicity parameter α_f similar to the sunspots of the solar cycle. Such results have also been reported in another study by Zhang *et al.* (2010) in their data obtained from other sources.

In order to get the time dependent hemisphere distribution of the parameter α_f , we ran a boxcar of width 90 days and counted the numbers of ARs following the HSR in both the hemispheres. Figure 3(d) shows the boxcar averaged hemispheric distribution of the parameter α_f . This plot shows that the ARs on average follow HSR for the magnetic helicity parameter α_f except at peak and end phase of the cycle for northern and southern ARs, respectively. The opposite hemispheric trend during the decay phase of this solar cycle has been found in earlier studies (*e.g.*, Bao, Ai, and Zhang, 2000; Tiwari, Venkatakrishnan, and Sankarasubramanian, 2009; Pipin *et al.*, 2019).

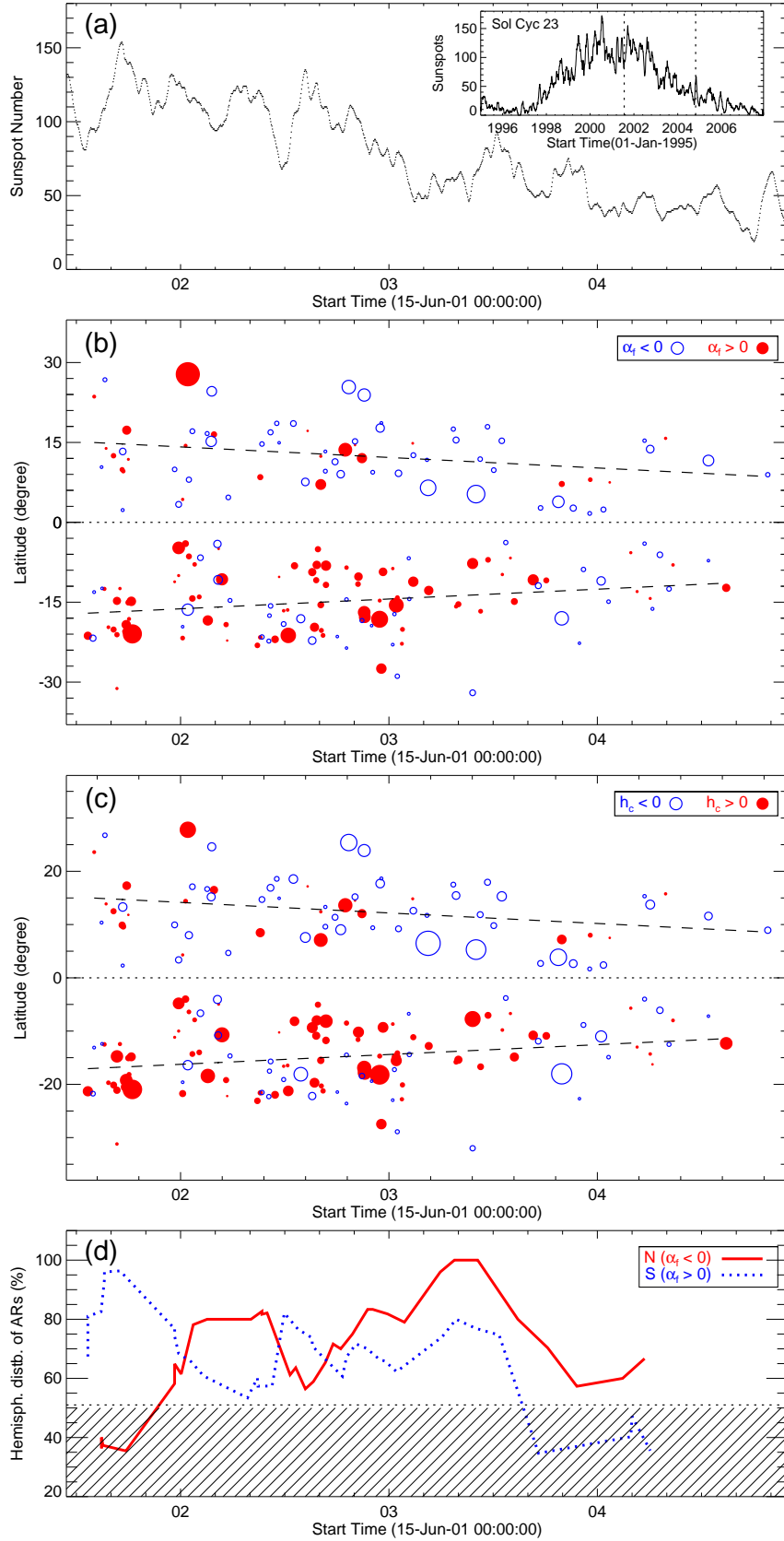


Figure 3. (a) Sunspot number as a function of time for reference. The complete sunspot cycle 23 is shown in the inset, where vertically dashed lines mark the time period of ARs which are analyzed in this paper. (b) Latitudinal distribution of magnetic helicity parameter α_f as a function of time, where sizes of opened (filled) circles represent magnitudes of negative (positive) values of the parameter α_f , and dashed lines represent the linear regression lines through ARs latitude. (c) Similar to the panel (b) but for the current helicity parameter h_c . (d) Hemispheric distribution of ARs as a function of time for northern (solid) and southern (dotted) hemispheres.

Table 1. Hemispheric distribution of topological parameters. For the actual values of the parameters listed in the columns 6-9, the multiplication factors, 10^{-8} , 10^{-3} , 10^{-9} and 10^{-15} should be applied for α_f , h_c , h_k and C_k , respectively.

Parameter (P)	N/S	HSR (%)	HSR (no.)	Total (no.)	Slope ($\times 10^{-2} deg^{-1}$)	Average	PDF Max.	PDF FWHM
α_f (m^{-1})	N	68	48	71	-3.4	-0.5	-0.5	2.3
	S	67	79	118				
h_c ($G^2 m^{-1}$)	N	68	48	71	-2.0	-0.3	-0.4	1.3
	S	68	80	118				
h_{k1} (ms^{-2})	N	65	46	71	-1.8	-0.3	-0.2	2.0
	S	56	66	118				
h_{k2} (ms^{-2})	N	69	49	71	-12.4	-1.9	-0.7	8.1
	S	67	79	118				
C_{k1} (s^{-2})	N	65	46	71	-2.4	-0.4	-0.3	2.2
	S	55	65	118				
C_{k2} (s^{-2})	N	65	46	71	-2.5	-0.4	-0.2	1.8
	S	70	83	118				

Table 2: Slopes of the distributions of the topological parameters (columns 2nd and 3rd) and their hemispheric distributions (columns 4th and 5th) as a function of B . For the actual values of the parameters listed in the columns 1-2, the multiplication factors, 10^{-8} , 10^{-3} , 10^{-9} and 10^{-15} should be applied for α_f , h_c , h_k and C_k , respectively.

Parameter (P)	+ve P (G^{-1})	-ve P (G^{-1})	HSR-N ($\times 10 G^{-1}$)	HSR-S ($\times 10 G^{-1}$)
$\alpha_f(m^{-1})$	5.6	-5.8	0.6	1.0
$h_c(G^2 m^{-1})$	5.1	-5.8	0.6	1.0
$h_{k1}(ms^{-2})$	0.1	-0.1	1.9	1.1
$h_{k2}(ms^{-2})$	1.4	-1.3	-1.1	-1.2
$C_{k1}(s^{-2})$	0.8	-3.0	0.9	1.2
$C_{k2}(s^{-2})$	1.6	-2.6	-0.7	-0.9

3.1.2. Current Helicity

Next, we analysed the current helicities h_c of all the 189 ARs similar to the magnetic helicity parameter α_f (see Section 3.1.1). The results of our analysis are shown in Figures 1 – 3. Figure 1(c) shows the latitudinal distribution of the vertical current helicity h_c . There are 68% ARs in both northern and southern hemispheres with negative and positive current helicities h_c , respectively. The small deviation in h_c from α_f for the southern ARs is due to averaging of h_c values for ARs that are observed multiple times. The values of h_c show a similar hemispheric trend as the force-free parameter α_f (Figure 1a). The slope of linear least square fit through h_c of ARs is found to be $-2.0 \times 10^{-10} Gm^{-1} degree^{-1}$. This hemispheric trend of ARs based on h_c confirms the earlier reports (Abramenko, Wang, and Yurchishin, 1996, and others).

The probability distribution function for h_c is shown in Figure 1(d). This shows hemispheric trend for h_c as the PDFs for northern and southern hemispheric ARs peak at $-4.1 \times 10^{-4} G^2 m^{-1}$ and $+1.8 \times 10^{-4} G^2 m^{-1}$, respectively. The FWHM of PDF for northern hemisphere is $1.3 \times 10^{-3} G^2 m^{-1}$ and for the southern hemisphere $1.5 \times 10^{-3} G^2 m^{-1}$. The PDF profiles of the parameter h_c and the parameter α_f are look-alike representing similar distributions of two topological parameters in ARs.

Figure 2(c) shows the variation of current helicity h_c as a function of absolute magnetic flux (B). It is found that h_c increases on increasing the magnetic flux of ARs similar to the magnetic helicity parameter α_f (Figure 2a). The slope of the linear least square fitting is found to be $5.1(-5.8) \times 10^{-6} Gm^{-1}$ for the positive (negative) h_c values of ARs. This

suggests that the ARs with stronger magnetic fields may have more current helicity than typical ARs. Figure 2(d) shows the hemispheric distribution of the current helicity h_c as a function of B , similar to Figure 2(b) for the helicity parameter α_f . It shows that the HSR becomes stronger with the magnetic field strength B as the slopes for northern(southern) ARs is found to be 0.06(0.10).

We have also analyzed the solar cyclic variation in the current helicity h_c . Figure 3(c) shows the hemispheric distribution of the current helicity parameter h_c as a function of time. This plot further confirms the equator-ward propagation of helicity h_c patterns. Since h_c has same sign as α_f , it shows similar time dependent distribution as shown in Figure 3(d) for the parameter α_f .

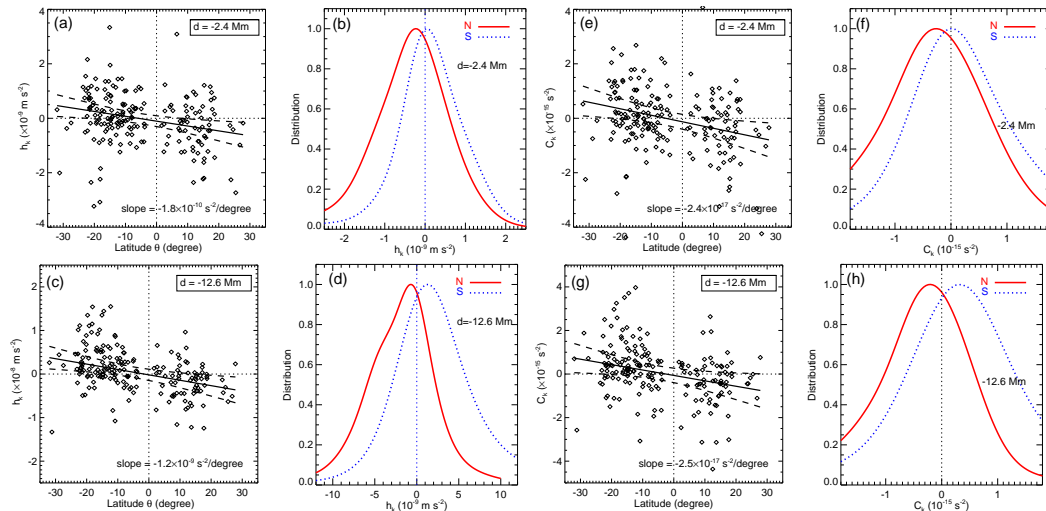


Figure 4. Similar to Figure 1 but for the kinetic helicity density h_k (first two columns) and divergence-curl C_k (last two columns) at two different depths 2.4 Mm (top row) and 12.6 Mm (bottom row).

3.2. Sub-photospheric Flow Fields

Helicities in the sub-photospheric velocity fields in our sample of 189 ARs are studied by computing the kinetic helicity density h_k (Equation 14) and the divergence-curl C_k (Equation 16). In Figures 4 – 9, we explain our results based on these parameters.

3.2.1. Kinetic Helicity Density

Figure 4(a-d) shows the latitudinal distribution of the vertical kinetic helicity h_k for depths 2.4 Mm (a) and 12.6 Mm (c). There is a clear hemispheric preference in the parameter h_k as there are 65%(56%) ARs at depth of 2.4 Mm and 69%(67%) ARs at depth of 12.6 Mm in the northern (southern) hemisphere having negative(positive) values. The linear regression through ARs shows slopes of $-1.8 \times 10^{-10} \text{ s}^{-2} \text{ degree}^{-1}$ for the depth of 2.4 Mm and $-1.2 \times 10^{-9} \text{ s}^{-2} \text{ degree}^{-1}$ for the depths of 12.6 Mm. These results show that the kinetic helicity have same hemispheric preference as that of magnetic helicity α_f and current helicity h_c . The larger values of h_k for deeper layers indicate that the parameter h_k have better hemispheric preference at larger depths.

To further confirm the hemispheric preference of kinetic helicity h_k , we have computed the PDF for the parameter h_k of northern and southern ARs. Figures 4(b) and 4(d) shows the PDF of h_k for the depths 2.4 Mm and 12.6 Mm. The PDF for h_k peaked at $-0.2(+0.1) \times 10^{-9} \text{ m s}^{-2}$ for northern (southern) hemispheric ARs for the depth 2.4 Mm. Similarly, the PDF for h_k at the depth 12.6 Mm peaked at $-0.7(+1.1) \times 10^{-9} \text{ m s}^{-2}$ which further confirms the HSR for parameter h_k .

In order to check depth dependent HSR for h_k , we computed the PDFs for all the available depths and plotted in Figure 5(a). We have also estimated the h_k associated with peaks of PDFs and displayed in Figure 5(b). We find that the peak position shifted towards larger h_k values at larger depths for both hemispheric ARs. The southern ARs show larger h_k values than northern ARs at deeper layers (> 6 Mm) but at shallower depths (< 6 Mm) northern

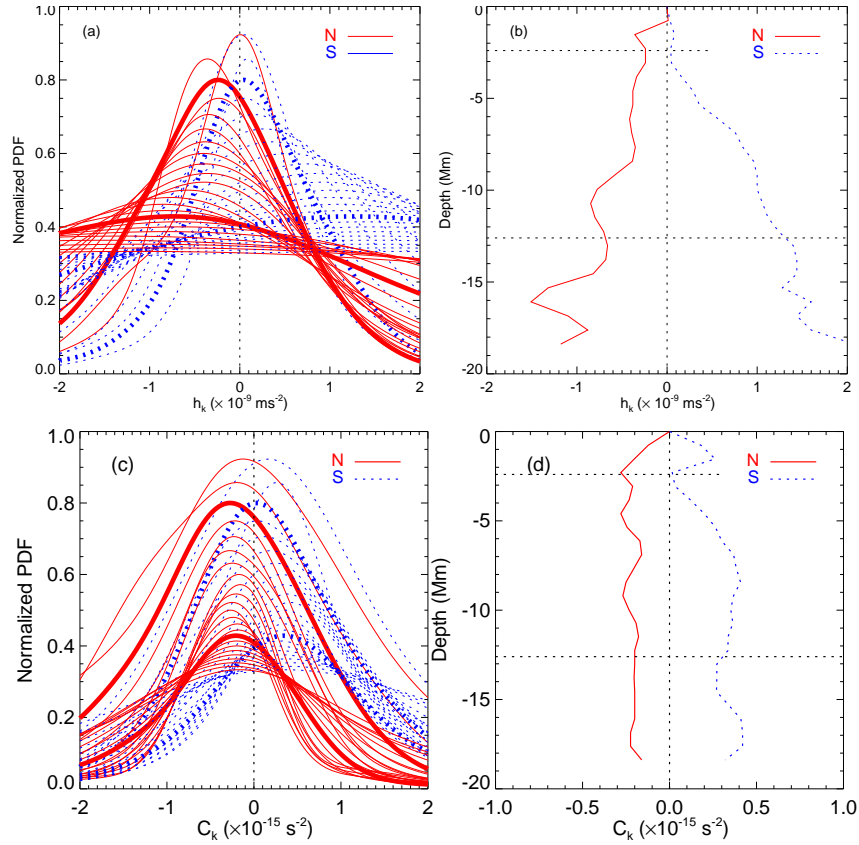


Figure 5. (a) Hemispheric probability density function for the sub-photospheric flow parameter h_k for several depths. The PDF is scaled down for deeper layers. Thick curves correspond to depths of 2.4 Mm and 12.6 Mm (b) The peak point of the PDFs (in panel a) as a function of depth. Bottom row is similar to the top row but for the parameter C_k .

ARs have larger h_k values than southern ARs. This could be due to stronger swirls in the sub-photospheric flows at deeper layers than shallower.

We have also analysed the variations in the kinetic helicity as a function of magnetic flux B . For this, we computed the slope of the distribution of h_k vs B as a function of depth (Figure 6a). We found that the magnitude of the slope enhances considerably at larger depths > 3 Mm for both positive and negative helicities. For example, the slope for

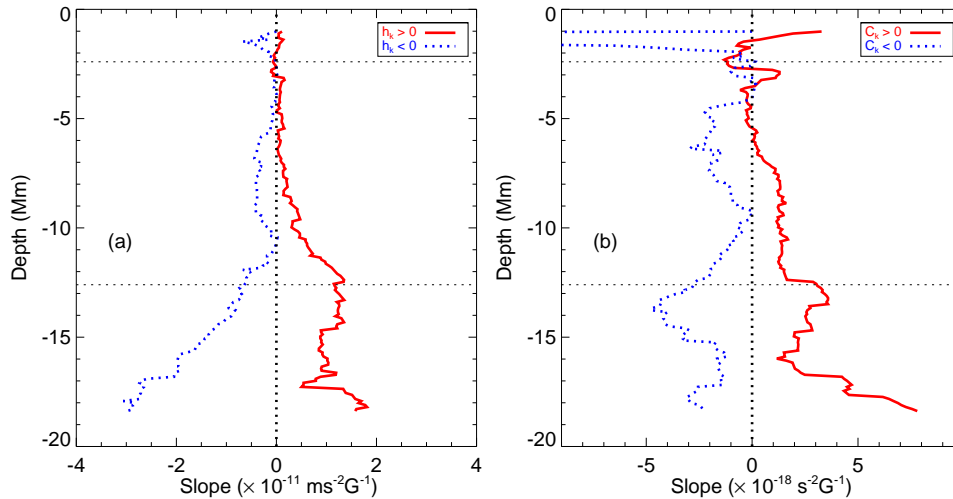


Figure 6. Variation in the slopes of the distribution of kinetic helicity h_k (a) and divergence-curl C_k (b) vs B as a function of depth for $h_k > 0$ (solid and red) and $h_k < 0$ (dotted and blue).

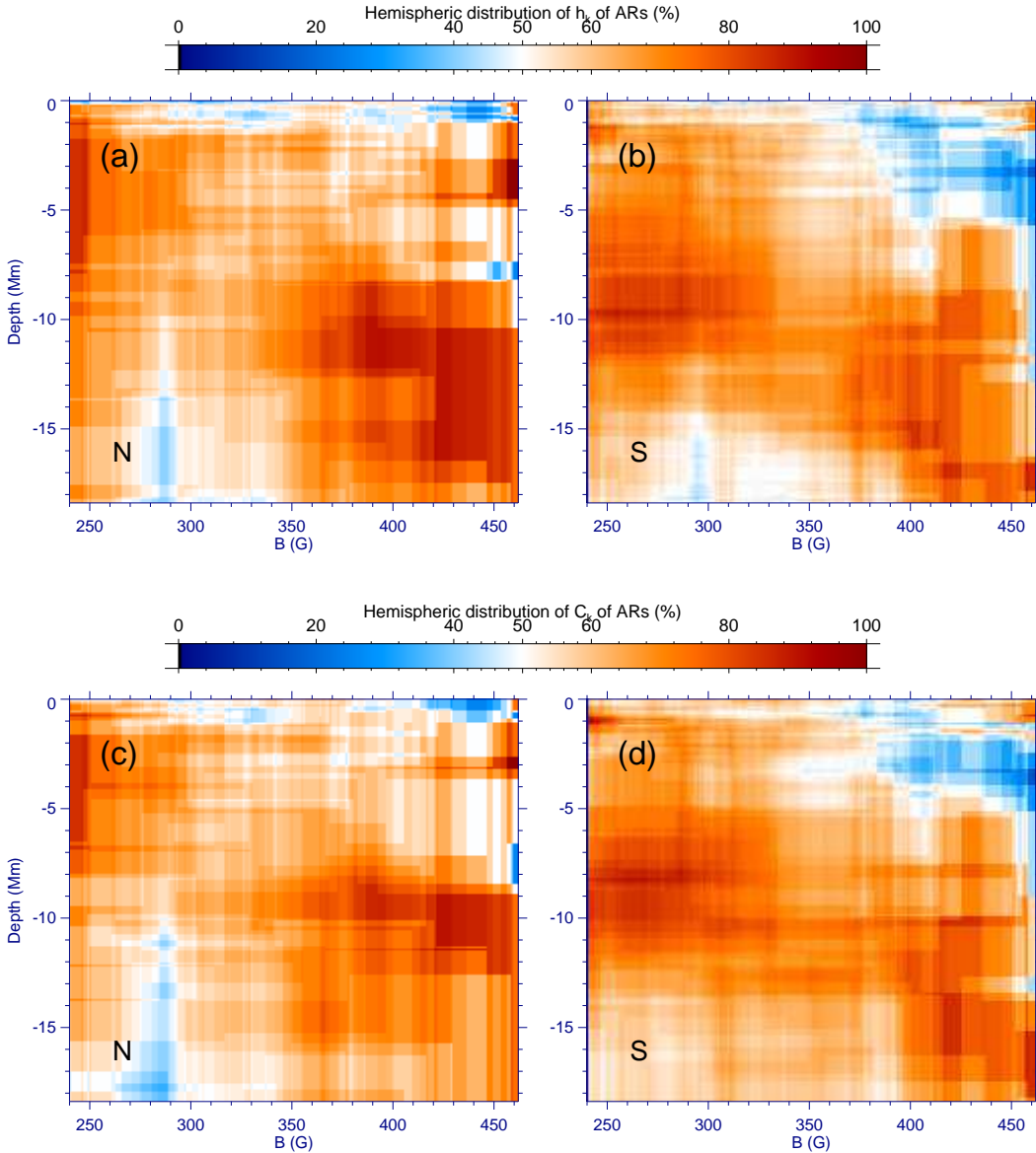


Figure 7. (Top row) Hemispheric distribution of sub-photospheric flow parameters h_k for northern (a) and southern (b) hemisphere, as a function of depth and magnetic flux B . (Bottom row) Similar to the top row but for the parameter C_k .

the depth 2.4 Mm is found to be $+1.9(+1.1) \times 10^{-10} m s^{-2}$ for positive(negative) h_k values while it increased to $+1.4(-1.3) \times 10^{-9} m s^{-2} G^{-1}$ at the depth of 12.6 Mm. The positive (negative) values of slope for the parameter $h_k > 0 (h_k < 0)$ represent the linear relation between the helicity parameter h_k and B . Similar result has been found for the magnetic helicity (Figure 2b) and the current helicity (Figure 2d).

Next, we find the hemispheric distribution of the parameter h_k as a function of depth and magnetic flux. For this we counted the number of ARs following the HSR by running a magnetic flux window of width 50 G for all depths. These results are shown in Figure 7 (top row) for northern (left panel) and southern (right panel) hemispheres. This clearly shows that the HSR, statistically, becomes stronger at larger depths. Also, as the magnetic flux B increases the hemispheric biases of ARs shifted towards larger depths. However, in ARs with smaller fluxes show opposite HSR trend in both hemispheres. Similar preference is also discernible at shallower layers in ARs having stronger fluxes. The increase in hemispheric preference of with magnetic flux has also been found for the photospheric magnetic helicity α_f (Figure 2b) as well as for the current helicity h_c (Figure 2d).

Figure 8(b) and 9(b) show the time dependent variations in the kinetic helicity parameter h_k for the depths 2.4 Mm and 12.6 Mm, respectively. The hemispheric biases are noticeable during the peak to decay phase of the solar cycle. But, these preferences are slightly weaker than the magnetic and current helicity parameters. The kinetic helicity h_k is found to be scattered significantly for both depths throughout the time period considered in the analysis. The magnitude of kinetic helicity of all ARs for the depth of 12.6 Mm are found to be larger throughout than that for the depth of 2.4 Mm. This shows largely variant sub-photospheric twisted flows in the interior of ARs. We could not find clear signature of equator-ward propagation of ARs for the parameter h_k at both depths.

In the first half year of 2003, the ARs in northern hemisphere deviated largely from usual HSR for the depth of 2.4 Mm (Figure 8d). Similarly, southern ARs show opposite HSR during November 2002 to January 2003. For the depth of 12.6 Mm (Figure 8d), the ARs show better HSR even during the aforesaid period. Southern ARs show better HSR than northern ARs from the peak to decay phase of the solar cycle. But, at the end phase of the solar cycle, some ARs in southern hemisphere were found to have opposite hemispheric trend.

3.2.2. Divergence-Curls of Sub-photospheric Flows

Figure 4(e-h) shows the latitudinal distribution of sub-photospheric flow parameter C_k for depths 2.4 Mm (e) and 12.6 Mm (g). For the above two depths, the latitudinal distributions of ARs are found to be 65%(55%) and 65%(70%) in the northern (southern) hemispheres having negative (positive) values of C_k . We noticed that the hemispheric distribution of ARs for C_k and h_k are same for the depth 2.4 Mm but different for the depth of 12.6 Mm. This is due to averaging of topological parameters of same ARs observed multiple times. The linear regression through distribution of the parameter C_k shows a slope of $-2.4 \times 10^{-17} s^{-2} degree^{-1}$ for the depth of 2.4 Mm and $-2.5 \times 10^{-17} s^{-2} degree^{-1}$ for the depth of 12.6 Mm. These results show hemispheric preferences similar to the magnetic helicity parameter α_f (Figure 1a), current helicity h_c (Figure 1c) and the kinetic helicity parameter h_k (Figure 4a and c).

The probability density function for the sub-photospheric flow parameters C_k is shown in Figures 4(f) for the shallower depth at 2.4 Mm and 4(h) for the deeper layer at 12.6 Mm. For the depth 2.4 Mm the parameter C_k peaks at $-2.5(+0.0 \times 10^{-16}) s^{-2}$ and for the depth 12.6 Mm it peaks at $-2.0(+3.6 \times 10^{-16}) s^{-2}$ for the northern (southern) hemisphere while average values of C_k were found to be $-4.2(+0.22) \times 10^{-16} s^{-2}$ for the depth of 2.4 Mm and $-0.43(+0.34) \times 10^{-15} s^{-2}$ for the depth of 12.6 Mm. This further confirms the HSR in C_k for the sub-photospheric flows of ARs.

Figure 5(c) shows depth dependent PDF for the parameter C_k for northern (red) and southern (blue) hemispheres similar to Figure 5 (a) for the kinetic helicity h_k . Figure 5(d) represents the variations in peak position of PDF for northern (red) and southern (blue) hemispheres as function of depth. The hemispheric distribution for the parameter C_k is found to exist for all depth range 0 – 20 Mm. At depths beyond 2.0 Mm it is significant as evident from Figure 5(d). The peaks of PDFs, between depth range 5 – 20 Mm, for both hemispheres are found to be nearly constant at $-2.0(+3.5) \times 10^{-16} s^{-2}$ for northern (southern) hemisphere while it shifted towards larger values at larger depth for the parameter h_k . The constant distribution of maximum peak of PDF of C_k is due to horizontal divergence. The flows are found to be largely diverging near the photosphere than in deeper layers. Hence increase in vorticity is compensated by decrease in divergence and results into constant value for the parameter C_k .

In order to study the variation in the topological parameter C_k as a function of depth and magnetic fields, we computed the slope of the distribution, C_k vs. B . The results are shown in the Figure 6(b) for $C_k > 0$ (solid and red curves) and $C_k < 0$ (dotted and blue curves). For example, the slope for $C_k > 0$ ($C_k < 0$) for the depth of 2.4 Mm is found to be $+0.78(-3.04) \times 10^{-18} s^{-2} G^{-1}$ while it changed to $+1.61(-2.63) \times 10^{-18} s^{-2} G^{-1}$ for the depth of 12.6 Mm. The slopes, on average, are found to increase as we go deeper ($> 4 Mm$).

Similar to the helicity h_k (Figure 7, top row), we computed the depth and magnetic field dependent hemispheric preference of the parameter C_k . This result is shown in Figure 7(bottom row). It clearly shows that the hemispheric distribution of C_k shifted towards

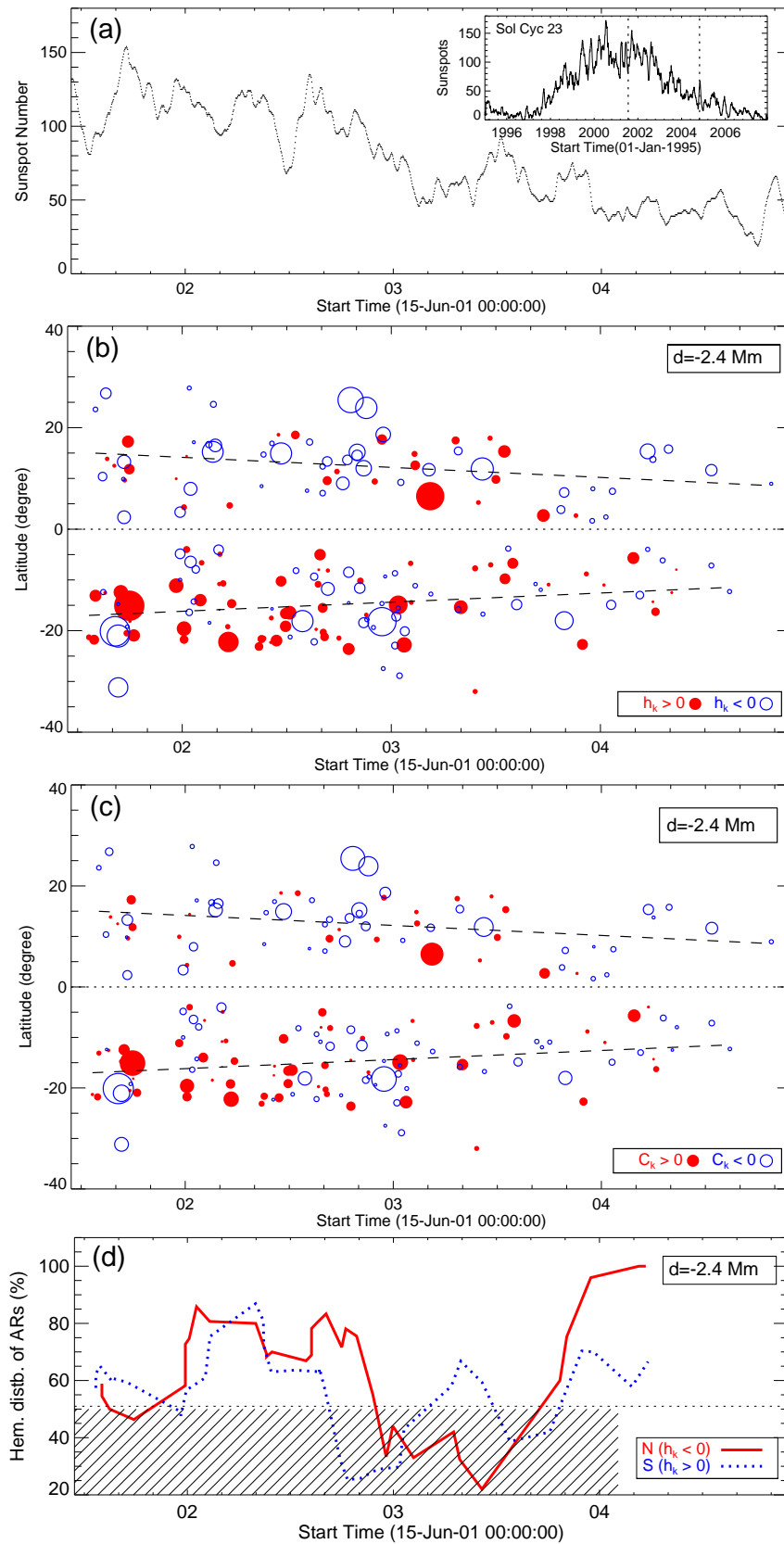


Figure 8. Similar to Figure 3 but for the parameters h_k and C_k at depth 2.4 Mm.

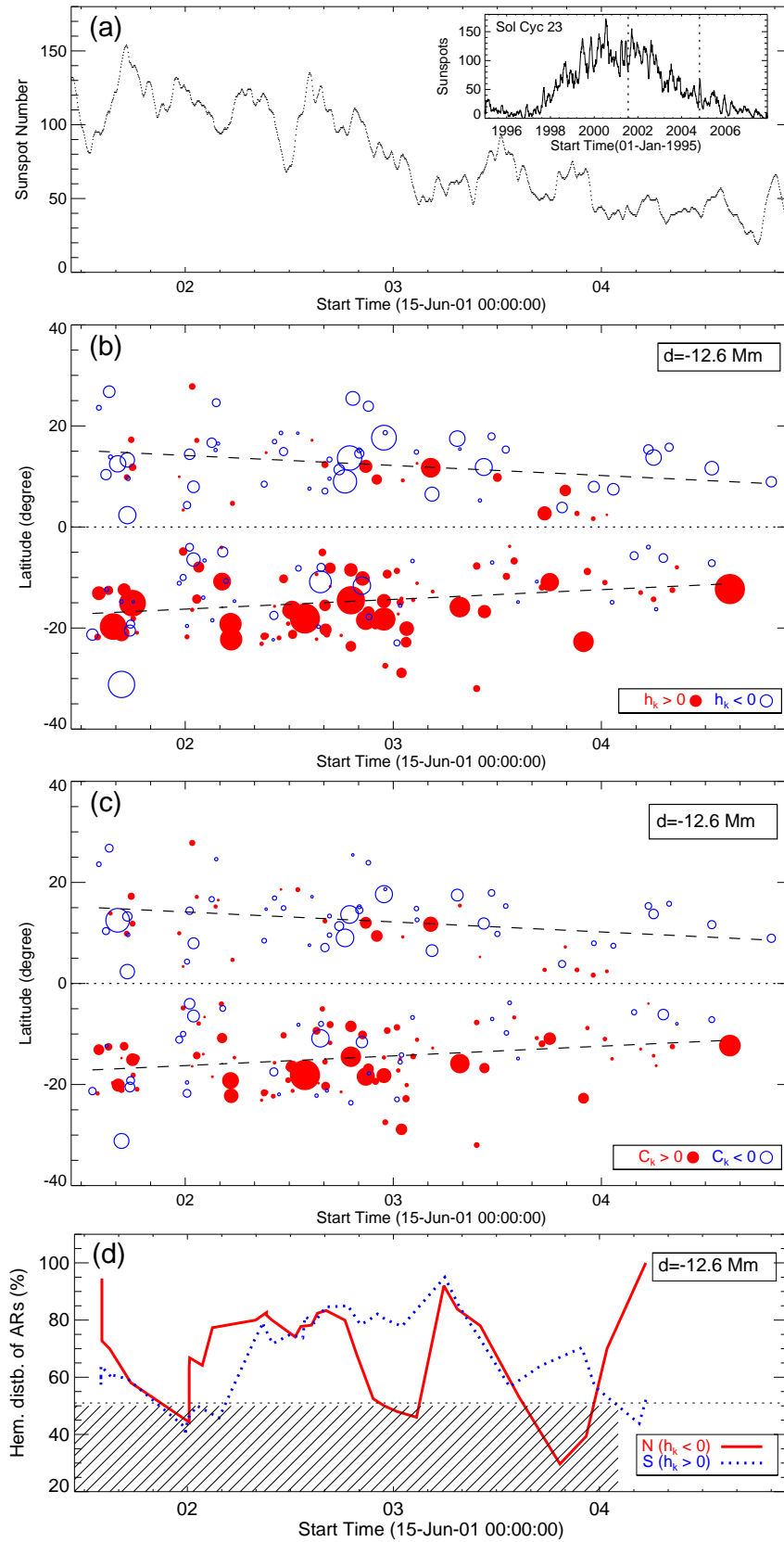


Figure 9. Similar to Figure 9 but for the depth 12.6 Mm.

larger depths as the magnetic field increases. Also, it can be noticed that the HSR became stronger with depth and magnetic flux B . Near the photosphere with stronger flux regions and deeper layers with smaller fluxes, the opposite hemispheric trends have been found in both the hemisphere. The hemispheric preference for the parameter C_k is very similar to that of h_k (Figure 7, top row) with same sign of handedness.

In order to check the solar cyclic variation of the parameter divergence-curl (C_k), we have plotted it as a function of time for two depths 2.4 Mm (Figure 8c) and 12.6 Mm (Figure 8c). We found that most of ARs shows C_k around an absolute mean of $1.0 \times 10^{-15} s^{-1}$ for both the depths. We found that the parameter C_k ranges between $\pm 4 \times 10^{-15} s^{-2}$ for both the depths (Figure 8c and 8c) while h_k (Figure 8b and 8b) have larger ranges for deeper depths. Similar to the parameter h_k , we did not find clear evidence of equator-ward propagation of the parameter C_k .

3.3. Relation between Kinetic and Magnetic Helicities

The relation between the surface and sub-surface helicities are shown in Figures 10 – 11. Figure 10(top row) shows the correlation between the force-free parameter α_f and the sub-photospheric twist parameters for the parameters h_k (a and c) and C_k (b and d) for two depths 2.4 Mm (a and b) and 12.6 Mm (c and d). The parameter α_f shows correlations with C_k and h_k at both depths. The correlation coefficient is significantly larger for deeper layer than the shallower. The significant values of the correlation coefficient CC shows relation between the two topological parameters of the surface magnetic fields and the sub-photospheric flows.

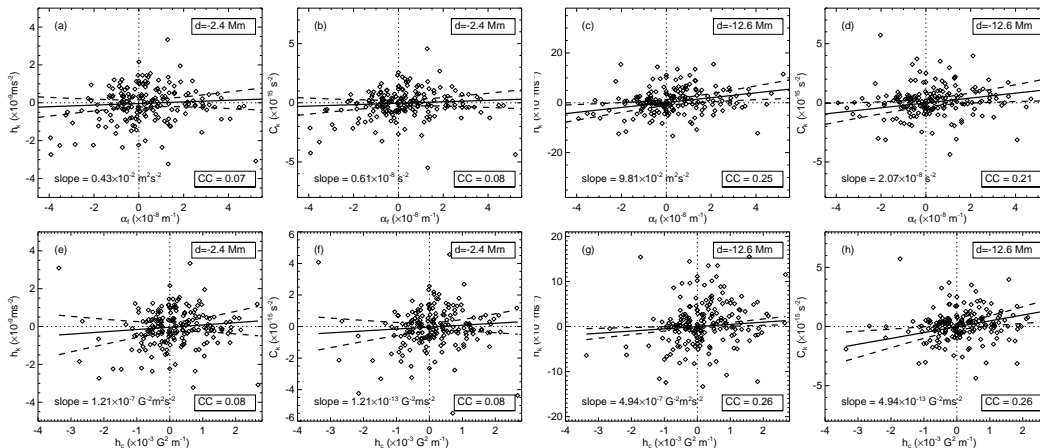


Figure 10. (top row) Kinetic helicity parameters h_k and C_k for two depths 2.4 Mm (a and b) and 12.6 Mm (c and d), as a function of magnetic helicity parameter α_f , where the values of CC represent the Pearson correlation coefficients between the topology of photospheric magnetic fields and sub-photospheric flows. Bottom row is similar to the top row but as a function of current helicity h_c .

Figure 10(bottom row) shows correlation between the current helicity and the twist parameter of sub-photospheric flows similar to Figure 10(top row) for the parameter α_f and sub-photospheric flow parameters h_k and C_k . Corresponding correlation coefficients are given in respective panels. The magnitudes of correlations imply association between the current helicity and the twist of sub-photospheric flows of ARs.

In order to check the depth dependent association between topology of photospheric magnetic fields and sub-photospheric flows, we have computed the correlation coefficients between magnetic and flows helicities parameters as a function of depth. The result is shown in Figure 11.

An interesting pattern of CC with depth is that it is not random. It changes gradually with depths. Very near the photosphere the sub-photospheric flows and magnetic fields topology show no significant relation as the CC is close to zero. But the absolute CC gradually increases with depth up to around of 1.5 Mm, then decreases and becomes minimum around a depth of 3.3 Mm, and thereafter starts increasing. There is a sharp increase

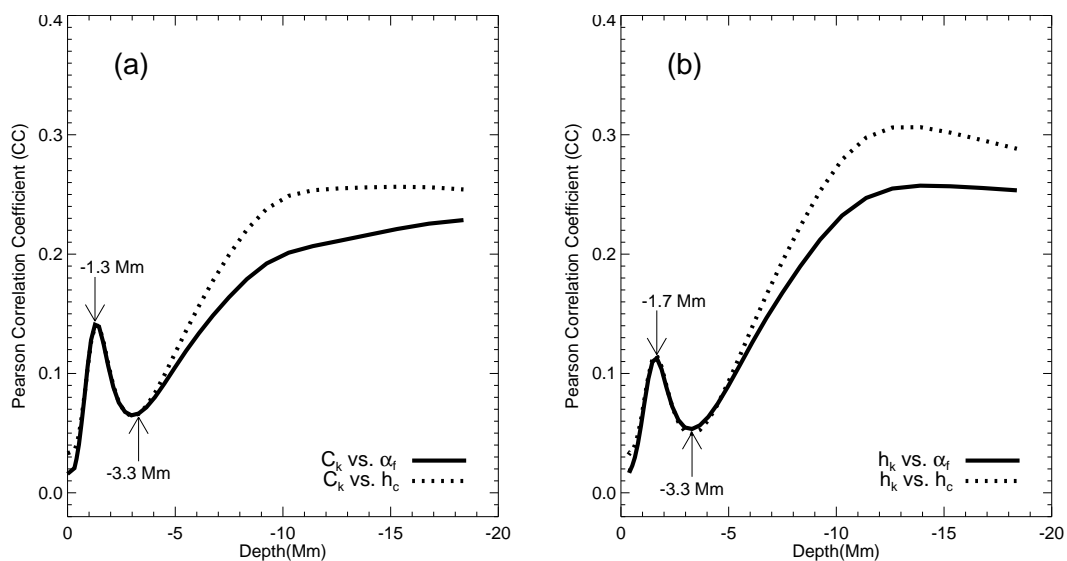


Figure 11. Depth dependent correlation coefficients between kinetic helicity and magnetic helicity parameters: (a) C_k & α_f (solid line), C_k & h_c (dashed line), (b) h_k & α_f (solid line), h_k & h_c (dashed line).

in CC between 3.4 – 12 Mm and after that it becomes almost constant. This shows that the photospheric magnetic field lines and the sub-photospheric flows at larger depths have similar topological trend. The two peaks in the CC -profile indicates the bi-polar structure in the sub-photospheric flows as reported earlier (Komm *et al.*, 2005; Maurya, Ambastha, and Tripathy, 2009; Maurya and Ambastha, 2010).

Another, interesting pattern of CC is that at larger depths (> 5 Mm) the magnitude of CC between current helicity and sub-photospheric topology is larger than the magnitude of CC between force-free parameter α_f and sub-photospheric topology parameters. This shows that the current helicity has association with the sub-photospheric flows topology. This is also evident from the mean field dynamo (Biskamp, 2003).

The gradual variation of CC between surface and sub-surface helicities could be due to the relation between the magnetic field and sub-photospheric flows. But, one should note that we are comparing the topology of magnetic field at the photosphere and the flows at depths. Since, there is no direct measurement of magnetic field in sub-photospheric depths, we cannot confidently suggest their association with flows. But from the above results it suggests that they may have some relation.

4. Summary and Conclusions

Using MSFC vector magnetograms and GONG Dopplergrams observations, we have analyzed the topological properties of photospheric magnetic fields and sub-photospheric flow fields of 189 ARs that cover peak to descending phase of the solar cycle 23. Our analysis confirms previous reports, and show some new interesting results.

We found clear evidence of hemispheric preferences for the magnetic and current helicities. The ARs of the northern(southern) hemisphere are found with dominantly negative (positive) helicities which confirms earlier reports (Pevtsov *et al.*, 2008, and others). However, many ARs were found to show opposite hemispheric preferences, especially at beginning and end phase of the solar cycle as indicated in others studies (Bao, Ai, and Zhang, 2000; Tiwari, Venkatakrishnan, and Sankarasubramanian, 2009; Pipin *et al.*, 2019). One should note that in complex magnetic field regions magnetic helicity proxy α_f may deviate from the force-free field, *i.e.*, α_f may not be a true proxy for helicity in complex sunspot regions to correctly reflect the twistedness of an AR as conjectured by Russell *et al.* (2019).

We have also found signature of equator-ward propagating pattern in the magnetic and current helicities similar to sunspots, in both hemispheres, during descending phase of the solar cycle. Zhang *et al.* (2010) have also reported similar results and suggested that the

solar dynamo could be helical in nature. An AR with larger area and stronger fields may have larger helicities. Therefore such patterns of helicities could also be due to variations of areas and magnetic fields of sunspots during a solar cycle, from larger areas with stronger fields regions to smaller areas with weaker field regions (Watson, Fletcher, and Marshall, 2011).

On comparing the magnetic and current helicity parameters with field strength of ARs, we found that the magnitude of both helicities increases. Another interesting pattern was found that the hemispheric preferences become stronger for both the helicity types, implying that ARs with larger field strengths show better hemispheric preferences. Hemispheric trend of current helicity infers that the regular vortex structure of sunspots is caused by forces such as the Coriolis and differential rotations.

In the sub-photospheric flows, we found similar hemispheric trend for the topological parameter, kinetic helicity h_k and divergence-curl C_k at all depths. Both the flow parameters follow same hemispheric preference as that of magnetic and current helicity parameters, *i.e.*, h_k and C_k are found to have dominantly negative (positive) sign in ARs of northern(southern) hemisphere. This confirms the earlier reports (Maurya, Ambastha, and Reddy, 2011; Seligman, Petrie, and Komm, 2014; Komm, Gosain, and Pevtsov, 2014; Komm and Gosain, 2015). But Gao, Zhang, and Zhao (2009) have found opposite hemispheric preferences in a small sample of ARs. Further, we could not detect clear signature of equator-ward propagating patterns in kinetic helicities of ARs as found for the magnetic helicities. Since kinetic and current helicities are related by mean field dynamo model such patterns are expected to exist in both the parameters.

The hemispheric preference of the parameter h_k could be due to mean field dynamo α_d (Biskamp, 2000, see Equation 5.19). Let us think of the hemispheric dependence of force-free alpha α_f , dynamo alpha α_d and kinetic helicity, $h_k = \langle \mathbf{u} \cdot \nabla \times \mathbf{u} \rangle \approx 3 \langle u_z (\nabla \times \mathbf{u})_z \rangle$. According to the mean-field dynamo, α_d and h_k are strongly related to each other by the relation $\alpha_d = -\frac{1}{3}\tau \langle \mathbf{u} \cdot \nabla \times \mathbf{u} \rangle = -\frac{1}{3}h_k\tau$, where τ is the velocity correlation time. Thus h_k and α_d have opposite signs. In the northern hemisphere, the Coriolis force causes a flow to be left-helical and $h_k < 0$. From our analysis, we have found statistically negative kinetic helicity for ARs which support the mean-field dynamo theory. Further, considering $h_k < 0$, we come to have $\alpha_d > 0$ in the northern hemisphere. This is commonly adopted view in the solar dynamo. It also seems to be consistent with Joy's law (Hale *et al.*, 1919). The condition of $\alpha_d > 0$ as well as the Joy's law suggests that the larger-scale magnetic field comprising bipolar ARs may be right helical. On the other hand, the force-free alpha α_f is empirically found to be negative in the northern hemisphere. This means that magnetic fields are left-helical in scales smaller than individual ARs.

The solar differential rotation may be another factor for the hemispheric trend of the sub-photospheric flows as rotation may introduce left- and right-handed vorticity in northern and southern hemispheres with magnitude of $0.01 \times 10^{-6} s^{-1}$ to $2.5 \times 10^{-6} s^{-1}$ for an AR of sizes 1 Mm to 40 Mm along the meridional direction.

The hemispheric preference for kinetic helicity is found to increase with depths. The magnitude of peak of kinetic helicity distribution is found to increase with depth for both hemispheric ARs while divergence-curl is found to be constant around depths 5 – 20 Mm. The reason for growth in kinetic helicity with depth is mainly due to increase in vertical velocity while constant value of the parameter C_k is caused by net effects of increase in swirl and decrease in divergence.

Our analysis shows interesting patterns of hemispheric preferences, of sub-photospheric flow topology, as a function of magnetic field strength and depths. The HSR for sub-photospheric flows topology enhances with magnetic field strength and with depths. Poor hemispheric preferences of flow topology near the photosphere, may be due to smaller plasma density and diverging magnetic field lines. This may be due to different scales of magnetic field lines. This supports the solar dynamo theory which predicts the bi-helical properties of magnetic fields (Blackman and Brandenburg, 2002; Brandenburg and Subramanian, 2005).

Further, we analysed the correlation between sub-photospheric flows and photospheric magnetic fields. The kinetic helicity, near the photosphere, do not show significant relation with magnetic or current helicities. But we found that the correlation between them enhances as we go deeper into the solar interior. The kinetic helicity and vertical divergence-curl show

correlation with magnetic and current helicities at all depths. Further, we found that the kinetic helicity shows better covariance with magnetic and current helicities than divergence-curl of flow fields, which supports the mean field dynamo models. Near-surface flow topology shows poor correlation with magnetic and current helicities. This suggests that the magnetic fields and flows may have different topologies. Another reason could be the frozen-in field conditions in the interior plasma, which may not be satisfied at these depths and results into weak association of magnetic and flow fields. But deeper into the interior there is increasingly high density plasma. There the field lines may be concentrated close to the flux tubes which may lead to similar topology in both physical quantities.

It should be noted that we have used a single (or a few) vector magnetograms map corresponding to an AR to derive the photospheric twist while the twist in sub-photospheric flow was obtained using the data cube for 1664 minutes. This could be one reason for weak relation between the photospheric magnetic fields and sub-photospheric flows. But magnetic helicity is likely to be approximately conserved in solar atmosphere on time scale of AR while passing the disc (Berger and Field, 1984). It should also be noted that we have used magnetic and Doppler fields observations obtained from different sources. These factors may be responsible in affecting our results and in reducing correlations of the twist parameters. It is expected that these results may improve in the future with magnetic and Doppler velocity observations obtained from the same instrument.

Acknowledgements This work utilizes data obtained by the GONG program operated by AURA, Inc. and managed by the National Solar Observatory under a cooperative agreement with the National Science Foundation, U.S.A. The vector magnetogram data were obtained from MSFC. This work also utilizes data from the Solar Oscillations Investigation/Michelson Doppler Imager (SOI/MDI) on the Solar and Heliospheric Observatory (SOHO). SOHO is a project of international cooperation between ESA and NASA. MDI was supported by NASA grants NAG5-8878 and NAG5-10483 to Stanford University. We are grateful to Prof. J. Chae of Seoul National University, South Korea for his valuable discussions and suggestions. R.A.M. thankfully acknowledge the support by the NITC/FRG-2019.

Disclosure of Potential Conflicts of Interest. The authors declare that they have no conflicts of interest.

References

- Abramenko, V.I., Wang, T., Yurchishin, V.B.: 1996, Analysis of electric current helicity in active regions on the basis of vector magnetograms. *Sol. Phys.* **168**, 75. DOI. ADS.
- Antia, H.M., Basu, S.: 2007, Local helioseismology using ring diagram analysis. *Astron. Nachr.* **328**, 257. DOI. ADS.
- Bao, S., Zhang, H.: 1998, Patterns of current helicity for the twenty-second solar cycle. *Astrophys. J. Lett.* **496**, L43. DOI. ADS.
- Bao, S.D., Ai, G.X., Zhang, H.Q.: 2000, The hemispheric sign rule of current helicity during the rising phase of cycle 23. *J. Astrophys. Astron.* **21**, 303. DOI. ADS.
- Berger, M.A., Field, G.B.: 1984, The topological properties of magnetic helicity. *J. Fluid Mech.* **147**, 133. DOI. ADS.
- Biskamp, D.: 2000, *Magnetic reconnection in plasmas*, Cambridge monographs on plasma physics **3**, Cambridge University Press, ISBN 0521582881. ADS.
- Biskamp, D.: 2003, *Magnetohydrodynamic Turbulence*, Cambridge University Press, ISBN 0521810116. ADS.
- Blackman, E.G., Brandenburg, A.: 2002, Dynamic nonlinearity in large-scale dynamos with shear. *Astrophys. J.* **579**(1), 359. DOI.
- Brandenburg, A., Subramanian, K.: 2005, Astrophysical magnetic fields and nonlinear dynamo theory. *Phys. Rep.* **417**(1-4), 1. DOI.
- Choudhuri, A.R.: 2003, On the connection between mean field dynamo theory and flux tubes. *Sol. Phys.* **215**(1), 31. DOI. ADS.
- Choudhuri, A.R., Chatterjee, P., Nandy, D.: 2004, Helicity of Solar Active Regions from a Dynamo Model. *Astrophys. J. Lett.* **615**(1), L57. DOI. ADS.
- Christensen-Dalsgaard, J., Dappen, W., Ajukov, S.V., Anderson, E.R., Antia, H.M., Basu, S., Baturin, V.A., Berthomieu, G., Chaboyer, B., Chitre, S.M., Cox, A.N., Demarque, P., Donatowicz, J., Dziembowski, W.A., Gabriel, M., Gough, D.O., Guenther, D.B., Guzik, J.A., Harvey, J.W., Hill, F., Houdek, G., Iglesias, C.A., Kosovichev, A.G., Leibacher, J.W., Morel, P., Proffitt, C.R., Provost, J., Reiter, J., Rhodes, E.J. Jr., Rogers, F.J., Roxburgh, I.W., Thompson, M.J., Ulrich, R.K.: 1996, The current state of solar modeling. *Science* **272**, 1286. DOI. ADS.

- Egorov, P., Rüdiger, G., Ziegler, U.: 2004, Vorticity and helicity of the solar supergranulation flow-field. *Astron. Astrophys.* **425**, 725. DOI. ADS.
- Elsasser, W.M.: 1956, Hydromagnetic dynamo theory. *Rev. Mod. Phys.* **28**(2), 135. DOI.
- Fan, Y., Zweibel, E.G., Linton, M.G., Fisher, G.H.: 1998, The rise of kink-unstable magnetic flux tubes in the solar convection zone. *Astrophys. J.* **505**(1), L59. DOI.
- Gao, Y., Zhang, H., Zhao, J.: 2009, Comparison of photospheric current helicity and subsurface kinetic helicity. *Monthly Not. RAS* **394**, L79. DOI. ADS.
- Gilman, P.A.: 1983, Dynamically consistent nonlinear dynamos driven by convection in a rotating spherical shell. ii - dynamos with cycles and strong feedbacks. *Astrophys. J. Sup.* **53**, 243. DOI. ADS.
- Gosain, S., Pevtsov, A.A., Rudenko, G.V., Anfinogentov, S.A.: 2013, First synoptic maps of photospheric vector magnetic field from solis/vsm: Non-radial magnetic fields and hemispheric pattern of helicity. *Astrophys. J.* **772**, 52. DOI. ADS.
- Gough, D.: 1985, Inverting helioseismic data. *Sol. Phys.* **100**, 65. DOI. ADS.
- Haber, D.A., Hindman, B.W., Toomre, J., Bogart, R.S., Thompson, M.J., Hill, F.: 2000, Solar shear flows deduced from helioseismic dense-pack samplings of ring diagrams. *Sol. Phys.* **192**, 335. ADS.
- Hagino, M., Sakurai, T.: 2004, Latitude variation of helicity in solar active regions. *Pub. ASJ* **56**, 831. ADS.
- Hagino, M., Sakurai, T.: 2005, Solar-cycle variation of magnetic helicity in active regions. *Pub. ASJ* **57**, 481. ADS.
- Hagyard, M.J., Pevtsov, A.A.: 1999, Studies of solar helicity using vector magnetograms. *Sol. Phys.* **189**(1), 25. DOI. ADS.
- Hagyard, M.J., Kineke, J.I.: 1995, Improved method for calibrating filter vector magnetographs. *Sol. Phys.* **158**, 11. DOI. ADS.
- Hagyard, M.J., Cumings, N.P., West, E.A., Smith, J.E.: 1982, The msfc vector magnetograph. *Sol. Phys.* **80**, 33. DOI. ADS.
- Hale, G.E.: 1927, The fields of force in the atmosphere of the sun. *Nature* **119**, 708. DOI. ADS.
- Hale, G.E., Ellerman, F., Nicholson, S.B., Joy, A.H.: 1919, The magnetic polarity of sun-spots. *Astrophys. J.* **49**, 153. DOI. ADS.
- Hill, F.: 1988, Rings and trumpets - three-dimensional power spectra of solar oscillations. *Astrophys. J.* **333**, 996. DOI. ADS.
- Holder, Z.A., Canfield, R.C., McMullen, R.A., Nandy, D., Howard, R.F., Pevtsov, A.A.: 2004, On the tilt and twist of solar active regions. *Astrophys. J.* **611**(2), 1149. DOI.
- Hood, A.W., Archontis, V., MacTaggart, D.: 2011, 3d MHD flux emergence experiments: Idealised models and coronal interactions. *Sol. Phys.* **278**(1), 3. DOI.
- Komm, R., Gosain, S.: 2015, Current and kinetic helicity of long-lived activity complexes. *Astrophys. J.* **798**, 20. DOI. ADS.
- Komm, R., Gosain, S., Pevtsov, A.A.: 2014, Hemispheric distribution of subsurface kinetic helicity and its variation with magnetic activity. *Sol. Phys.* **289**(7), 2399. DOI.
- Komm, R., Corbard, T., Durney, B.R., González Hernández, I., Hill, F., Howe, R., Toner, C.: 2004, Solar subsurface fluid dynamics descriptors derived from global oscillation network group and michelson doppler imager data. *Astrophys. J.* **605**, 554. DOI. ADS.
- Komm, R., Howe, R., Hill, F., González Hernández, I., Toner, C.: 2005, Kinetic helicity density in solar subsurface layers and flare activity of active regions. *Astrophys. J.* **630**, 1184. DOI. ADS.
- Komm, R., Howe, R., Hill, F., Miesch, M., Haber, D., Hindman, B.: 2007, Divergence and vorticity of solar subsurface flows derived from ring-diagram analysis of mdi and gong data. *Astrophys. J.* **667**, 571. DOI. ADS.
- LaBonte, B.J., Georgoulis, M.K., Rust, D.M.: 2007, Survey of magnetic helicity injection in regions producing x-class flares. *Astrophys. J.* **671**(1), 955. DOI.
- Leka, K.D., Skumanich, A.: 1999, On the value of ' α AR' from vector magnetograph data - I. Methods and Caveats. *Sol. Phys.* **188**(1), 3. DOI. ADS.
- Lim, E., Chae, J.: 2009, Chirality of intermediate filaments and magnetic helicity of active regions. *Astrophys. J.* **692**, 104. DOI. ADS.
- Liu, Y., Hoeksema, J.T., Sun, X.: 2014, Test of the hemispheric rule of magnetic helicity in the sun using the helioseismic and magnetic imager (hmi) data. *Astrophys. J. Lett.* **783**(1), L1. DOI.
- Longcope, D.W., Fisher, G.H., Pevtsov, A.A.: 1998, Flux-tube twist resulting from helical turbulence: The sigma-effect. *Astrophys. J.* **507**, 417. DOI. ADS.
- Martin, S.F., Bilimoria, R., Tracadas, P.W.: 1994, Magnetic field configurations basic to filament channels and filaments. In: Rutten, R.J., Schrijver, C.J. (eds.) *Solar Surface Magnetism*, 303. ADS.
- Maurya, R.A., Ambastha, A.: 2010, Sub-surface meridional flow, vorticity and the life time of solar active regions. *Astrophys. J. Lett.* **714**, L196. DOI. ADS.
- Maurya, R.A., Ambastha, A., Chae, J.: 2014, Activity related variations of high-degree p-mode amplitude, width and energy in solar active regions. *Astron. Astrophys.* **561**, A123. DOI. ADS.
- Maurya, R.A., Ambastha, A., Reddy, V.: 2011, Kinetic and magnetic helicities in solar active regions. *J. Phys. Conf. Ser.* **271**(1), 012003(1). DOI. ADS.
- Maurya, R.A., Ambastha, A., Tripathy, S.C.: 2009, Variations in p-mode parameters with changing onset time of a large flare. *Astrophys. J. Lett.* **706**, L235. DOI. ADS.
- Metcalf, T.R., Leka, K.D., Barnes, G., Lites, B.W., Georgoulis, M.K., Pevtsov, A.A., Balasubramaniam, K.S., Gary, G.A., Jing, J., Li, J., Liu, Y., Wang, H.N., Abramenko, V., Yurchyshyn, V., Moon, Y.: 2006, An overview of existing algorithms for resolving the 180 degree ambiguity in vector magnetic fields: Quantitative tests with synthetic data. *Sol. Phys.* **237**, 267. DOI. ADS.
- Miesch, M.S., Brun, A.S., DeRosa, M.L., Toomre, J.: 2008, Structure and evolution of giant cells in global models of solar convection. *Astrophys. J.* **673**(1), 557. DOI.
- Moffatt, H.K.: 1969, The degree of knottedness of tangled vortex lines. *J. Fluid. Mech.* **35**(1), 117. DOI.
- Moffatt, H.K., Tsinober, A.: 1992, Helicity in laminar and turbulent flow. *Annu. Rev. Fluid Mech.* **24**, 281. DOI. ADS.

- Pevtsov, A.A., Balasubramaniam, K.S., Rogers, J.W.: 2003, Chirality of chromospheric filaments. *Astrophys. J.* **595**, 500. [DOI](#). [ADS](#).
- Pevtsov, A.A., Canfield, R.C., Latushko, S.M.: 2001, Hemispheric helicity trend for solar cycle 23. *Astrophys. J. Lett.* **549**, L261. [DOI](#). [ADS](#).
- Pevtsov, A.A., Canfield, R.C., Metcalf, T.R.: 1995, Latitudinal variation of helicity of photospheric magnetic fields. *Astrophys. J. Lett.* **440**, L109. [DOI](#). [ADS](#).
- Pevtsov, A.A., Canfield, R.C., Sakurai, T., Hagino, M.: 2008, On the solar cycle variation of the hemispheric helicity rule. *Astrophys. J.* **677**, 719. [DOI](#). [ADS](#).
- Pipin, V.V., Pevtsov, A.A., Liu, Y., Kosovichev, A.G.: 2019, Evolution of magnetic helicity in solar cycle 24. *Astrophys. J. Lett.* **877**, L36. [DOI](#). [ADS](#).
- Priest, E.R.: 2014, A life of fun playing with solar magnetic fields (special historical review). *Sol. Phys.* [DOI](#). [ADS](#).
- Richardson, R.S.: 1941, The nature of solar hydrogen vortices. *Astrophys. J.* **93**, 24. [DOI](#). [ADS](#).
- Ronan, R.S., Orrall, F.Q., Mickey, D.L., West, E.A., Hagyard, M.J., Balasubramaniam, K.S.: 1992, A comparison of vector magnetograms from the marshall space flight center and mees solar observatory. *Sol. Phys.* **138**(1), 49. [DOI](#).
- Russell, A.J.B., Demoulin, P., Hornig, G., Pontin, D.I., Candelaresi, S.: 2019, Do current and magnetic helicities have the same sign? *Astrophys. J.* **884**(1), 55. [DOI](#).
- Seehafer, N.: 1990, Electric current helicity in the solar atmosphere. *Sol. Phys.* **125**, 219. [DOI](#). [ADS](#).
- Seligman, D., Petrie, G.J.D., Komm, R.: 2014, A combined study of photospheric magnetic and current helicities and subsurface kinetic helicities of solar active regions during 2006-2013. *Astrophys. J.* **795**, 113. [DOI](#). [ADS](#).
- Tiwari, S.K., Venkatakrishnan, P., Sankarasubramanian, K.: 2009, Global twist of sunspot magnetic fields obtained from high-resolution vector magnetograms. *Astrophys. J. Lett.* **702**, L133. [DOI](#). [ADS](#).
- Venkatakrishnan, P., Gary, G.A.: 1989, Off disk-center potential field calculations using vector magnetograms. *Sol. Phys.* **120**, 235. [DOI](#). [ADS](#).
- Watson, F.T., Fletcher, L., Marshall, S.: 2011, Evolution of sunspot properties during solar cycle 23. *Astron. Astrophys.* **533**, A14. [DOI](#). [ADS](#).
- West, E.A., Hagyard, M.J., Gary, G.A., Smith, J., Adams, M., Cloyd, R.A.: 2002, In: Goldstein, D.H., Chenault, D.B., Egan, W.G., Duggin, M.J. (eds.) *Development of a new vector magnetograph at Marshall Space Flight Center, Society of Photo-Optical Instrumentation Engineers (SPIE) Conference Series* **4481**, 270. [DOI](#). [ADS](#).
- Yang, S., Zhang, H., Büchner, J.: 2009, Magnetic helicity accumulation and tilt angle evolution of newly emerging active regions. *Astron. Astrophys.* **502**, 333. [DOI](#). [ADS](#).
- Zhang, H., Yang, S.: 2013, Distribution of magnetic helicity flux with solar cycles. *Astrophys. J.* **763**(2), 105. [DOI](#).
- Zhang, H., Sakurai, T., Pevtsov, A., Gao, Y., Xu, H., Sokoloff, D.D., Kuzanyan, K.: 2010, A new dynamo pattern revealed by solar helical magnetic fields. *Mon. Not. Roy. Astron. Soc.* **402**(1), L30. [DOI](#).
- Zhang, M.: 2006, Helicity observations of weak and strong fields. *Astrophys. J.* **646**(1), L85. [DOI](#).